Nano Research

Open Access

Research Article

Sustained single-textured zinc electrodeposition via organic–inorganic hybrid molecular design for high-capacity aqueous zinc-metal batteries

Haoran Du[1] ✉, Shanjie Zhang[1], Wenjuan Yang[1], Kunhong Hu[1], Lei Hu[1], Xinfeng Zhang[1], Yi Zhao[1], Wei Yang[1,2], Xin Liang[1] ✉, and Long Qie[3] ✉

[1] *Key Laboratory of Materials and Technologies for Advanced Batteries, School of Energy Materials and Chemical Engineering, Hefei University, Hefei 230601, China*
[2] *Anhui Provincial Key Laboratory of Urban Rail Transit Safety and Emergency Management, Hefei University, Hefei 230601, China*
[3] *State Key Laboratory of Material Processing and Die & Mold Technology, School of Materials Science and Engineering, Huazhong University of Science and Technology, Wuhan 430074, China*

Cite this article: *Nano Research*, **2026**, *19*, 94908661. https://doi.org/10.26599/NR.2026.94908661

ABSTRACT: The uncontrolled zinc electrodeposition in aqueous electrolytes, characterized by crystallographic randomness, remains a fundamental challenge due to dendritic growth and parasitic reactions. This work introduces a multifunctional organic–inorganic hybrid additive, magnesium bis(benzenesulfonyl)imide ($Mg(BBI)_2$), to precisely direct Zn deposition. The mechanistic studies reveal that the BBI^- anions preferentially adsorb onto the specific (101) and (100) Zn planes to block the nucleation sites of these two planes, thereby promoting a highly oriented deposition dominated by the (002) plane. Concurrently, the Mg^{2+} cations weaken the Zn^{2+}-SO_4^{2-}/H_2O interaction, serving as a long-term texture stabilizer for the single-textured electrodeposition. The tiny addition of $Mg(BBI)_2$ (0.02 M in 2 M $ZnSO_4$) achieves the Zn plating with a strikingly high (002) relative texture coefficient of 97.9% and superior corrosion resistance. Moreover, this hybrid molecular design represents a shift from the repurposing of existing molecules to purposefully functionalized synthesis, which endows durable high-zinc-utilization Zn||Zn symmetric cells and high-capacity full cells coupled with various cathodes, such as $CaV_6O_{16}\cdot 2.7H_2O$ cathodes with high mass loading (16 and 22.6 mg·cm^{-2}).

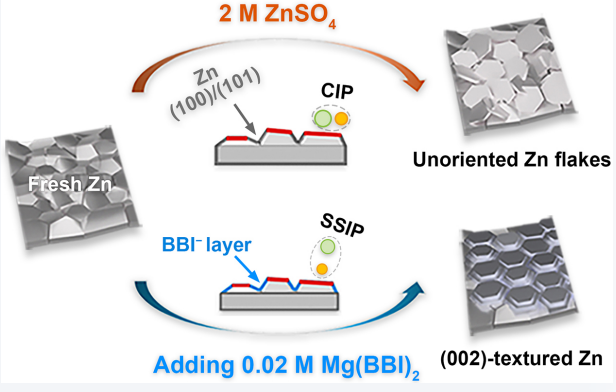

KEYWORDS: additive synthesis, dendrite-free, corrosion resistance, texture regulation, hybrid molecule

1 Introduction

Aqueous zinc-metal batteries (AZMBs) are regarded as a promising technology for stationary energy storage, capitalizing on their inherent safety, economic viability, and ecological friendliness [1–3]. Nevertheless, the practical application of Zn anodes in conventional mildly acidic electrolytes (such as 2 M $ZnSO_4$) is hampered by dendritic formation and corrosive degradation. These issues stem from unregulated electrodeposition and the intrinsic thermodynamic instability of Zn, leading to inadequate cycle life, serious gas evolution, and problematic interfacial passivation [4–6]. Therefore, devising a practicable approach to ensure dependable Zn electrodeposition is imperative for developing commercially viable AZMBs with extended calendar and cycling lifespans.

The pursuit of long-lasting Zn anodes has recognized crystallographic orientation control as a particularly straightforward strategy. The field gained significant development after Archer et al. reported an epitaxial Zn deposition process on graphene, a lattice-matched substrate for (002)-Zn [7]. This breakthrough ignited considerable interest in oriented plating, especially (002)-textured Zn, due to its demonstrated resistance against dendrites and parasitic reactions [8, 9]. Commercially Zn foils, however, are polycrystalline, composed of numerous randomly oriented grains

Received: February 6, 2026; **Revised:** March 3, 2026
Accepted: March 22, 2026

✉Address correspondence to Haoran Du, duhr@hfuu.edu.cn; Xin Liang, x.liang@hfuu.edu.cn; Long Qie, qie@hust.edu.cn

within a hexagonal close-packed (hcp) structure, predominantly exposing (002), (100), and (101) facets [10]. The Gibbs–Curie–Wulff theorem dictates that a crystal plane's growth velocity is proportional to its surface energy [11]. Therefore, the distinct surface energies of these various Zn facets present a fundamental barrier to achieving a uniform and single-textured deposit.

Many strategies have been explored to direct Zn electrodeposition orientation, encompassing mechanical rolling, thermal annealing, surface coatings, epitaxial substrates, electric field manipulation, and electrolyte engineering [12–16]. Among them, electrolyte engineering, especially additive engineering, is one of the relatively efficient strategies because of its operational simplicity and high effectiveness. A persistent challenge, however, is that even in optimized electrolytes, the plated Zn often retains a significant population of (101) and (100) grains, which have lower nucleation barriers. These grains serve as preferential sites for new nucleation, progressively undermining the plane selectivity over repeated cycling. Moreover, the inherently corrosive aqueous environment continuously attacks these exposed high-reactivity grains, further undermining the texture selectivity of Zn plating [17, 18]. Consequently, most conventional additives, which are often repurposed from existing molecules, fail to deliver both the efficacy and durability required for texture regulation, manifesting in an inability to achieve a sustained Zn plating with high relative texture coefficients (RTCs) of > 95%, as summarized in Table S1 in the Electronic Supplementary Material (ESM). It is imperative to transition towards a rational design of artificial additives with targeted functionalities to achieve precise and sustained control over Zn electrochemistry for single-textured deposition.

Herein, we designed a bifunctional organic–inorganic hybrid additive, magnesium bis(benzenesulfonyl)imide ($Mg(BBI)_2$), to simultaneously achieve highly (002)-textured and corrosion-suppressed Zn electrodeposition. *In-situ/ex-situ* characterizations visualized that the BBI^- anions selectively adsorbed onto the Zn surface, which kinetically suppresses the exposure of the (100) and (101) planes during plating/stripping cycles. Simultaneously, the Mg^{2+} cation weakened the interaction between Zn^{2+} and corrosive species (e.g., H_2O and SO_4^{2-}), thereby suppressing interfacial side reactions and ensuring the sustainability of the (002)-textured deposition. Thanks to the tiny 0.02 M $Mg(BBI)_2$, the Zn electrodes cycled in Zn||Zn symmetrical cells achieved an ultrahigh $RTC_{(002)}$ of 97.9%. These Zn||Zn symmetrical cells exhibited exceptional cycling stability: > 4000, > 1400, and > 300 h, corresponding to 2.1%, 10.4%, and 85.4% Zn utilization rate (ZUR), repectively. The practicability of this strategy was further demonstrated in high-performance full cells employing VS_2, $CaV_6O_{16}{\cdot}2.7H_2O$ (CVO), and polyaniline (PANI) as cathodes, even under challenging conditions such as high-loading CVO cathodes (16 and 22.6 $mg{\cdot}cm^{-2}$).

2 Results and discussion

2.1 Crystallographic characterizations of Zn electrodeposits

$Mg(BBI)_2$ was synthesized via straightforward neutralization of BBI and $Mg(OH)_2$ (Figs. S1 and S2 in the ESM), adapting the method we established previously for $Zn(BBI)_2$ [19]. The efficacy of this hybrid additive in promoting a highly (002)-textured Zn deposit is demonstrated in Fig. 1. As illustrated in the schematic of the hexagonal close-packed Zn crystal structure (Fig. 1(a)), the (002) plane is characterized by a flat and hexagonal arrangement of atoms [20]. To assess the texture evolution, we compared four electrolytes: a baseline 2 M $ZnSO_4$, and those modified with 0.02 M $MgSO_4$, $Zn(BBI)_2$, and $Mg(BBI)_2$. The crystalline structures of Zn electrodes cycled in Zn||Zn symmetric cells (5 $mA{\cdot}cm^{-2}$ and 5 $mAh{\cdot}cm^{-2}$) within these electrolytes were analyzed by X-ray diffractometer (XRD) (Fig. 1(b)). After 25 cycles, the XRD patterns from the $ZnSO_4$ and Zn-$MgSO_4$ electrolytes are nearly identical, indicating that Mg^{2+} alone has a negligible effect on Zn crystallization. In stark contrast, electrolytes containing BBI^- (both Zn-$Zn(BBI)_2$ and Zn-$Mg(BBI)_2$) produced deposits with a dominant (002) diffraction peak, its intensity far surpassing those of the (101) and (100) planes, which confirms that the BBI^- anion is the primary driver of crystallographic selectivity. The RTCs for the (002) plane, calculated from the XRD data, are summarized in Fig. 1(c). The $RTC_{(002)}$ obtained under the addition of $Mg(BBI)_2$ (97.9%) significantly outperforms the values obtained under the addition of $MgSO_4$ (32.9%) and bare $ZnSO_4$ electrolyte (36.2%). A similarly high $RTC_{(002)}$ of 97.8% was achieved with the Zn-$Zn(BBI)_2$ electrolyte, clearly demonstrating the superior ability of BBI-based additives to drive a (002)-preferred orientation, as benchmarked against recent literature (summarized in Fig. 1(d) and Table S1 in the ESM).

The macroscopic impact of electrolyte composition on deposit quality is immediately apparent in the digital photos of Zn electrodes after 25 cycles (Fig. 1(e)). Electrodes cycled in the $ZnSO_4$ and Zn-$MgSO_4$ electrolytes display a visibly rough and inhomogeneous surface. In sharp contrast, those from the Zn-$Zn(BBI)_2$ and Zn-$Mg(BBI)_2$ electrolytes are characterized by a smooth, flat, and lustrous appearance. This difference in morphology is further corroborated by scanning electron microscopy (SEM). The electrodes from the $ZnSO_4$ and Zn-$MgSO_4$ electrolytes (Figs. S3 and S4 in the ESM) are covered with a multitude of irregular and haphazard particles compared with the pristine Zn foil (Fig. S5 in the ESM). Conversely, the electrodes cycled in the presence of BBI^- anions (the Zn-$Zn(BBI)_2$ and Zn-$Mg(BBI)_2$ electrolytes, Figs. S6 and S7 in the ESM) retain a smooth and uniform surface, confirming the profound morphological regulation induced by the organic component. The long-term efficacy of texture control was investigated by extending the cycling to 100 cycles. Remarkably, the Zn plating obtained in the Zn-$Mg(BBI)_2$ electrolyte maintained its highly (002)-oriented texture (Fig. 1(f)). However, the electrode from the Zn-$Zn(BBI)_2$ electrolyte showed a significant degradation in texture consistency, with the emergence of numerous non-(002)-oriented grains (Fig. 1(g)). This critical divergence clarifies the indispensable role of Mg^{2+} in preserving the crystallographic integrity and ensuring the sustainability of the (002) texture over extended cycling. The absence of Mg^{2+} in the Zn-$Zn(BBI)_2$ electrolyte fails to provide such long-term texture stability, leading to gradual texture degradation and morphological roughening.

2.2 Corrosion resistance analysis

The long-term interfacial stability and phase composition of cycled Zn electrodes were illustrated by XRD after 100 cycles in Zn||Zn cells under 5 $mA{\cdot}cm^{-2}$ and 5 $mAh{\cdot}cm^{-2}$ (Fig. 2(a)). A pronounced peak at ~ 8°, attributable to $Zn_4SO_4(OH)_6{\cdot}xH_2O$ (ZSH), is evident in the pattern of the electrode cycled in the $ZnSO_4$ electrolyte, signifying severe parasitic reactions [21]. The intensity of ZSH-

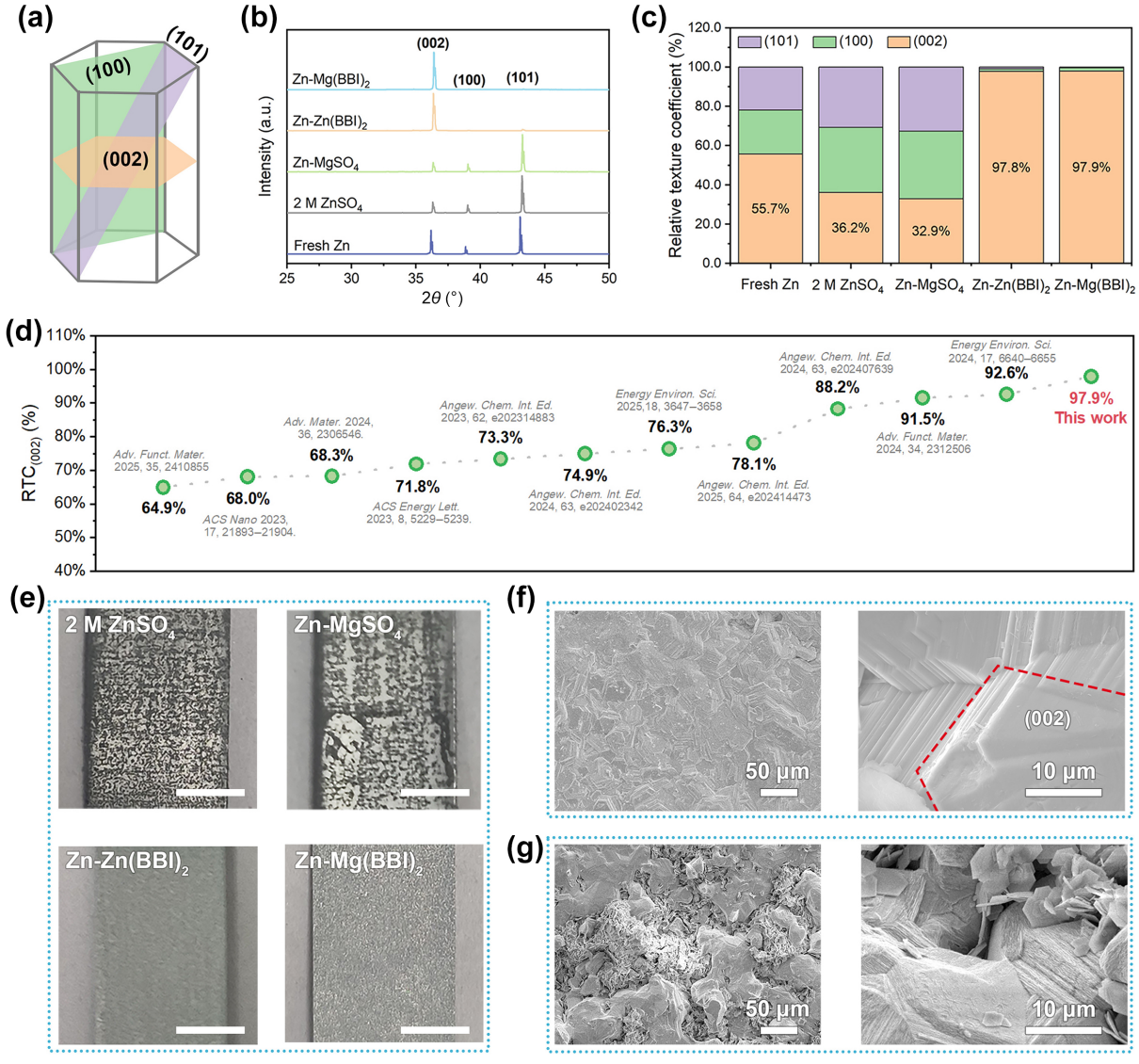

Figure 1 Crystallographic and morphological characterizations of Zn electrodeposits modulated by the $Mg(BBI)_2$ additive. (a) Schematic model of the (002), (101), and (100) crystal planes in the hcp Zn structure. (b) XRD patterns and (c) corresponding calculated RTCs for the (002) plane of pristine and cycled Zn electrodes (after 25 cycles in Zn||Zn cells at 5 $mA·cm^{-2}$ and 5 $mAh·cm^{-2}$). (d) Comparison of the $RTC_{(002)}$ value achieved in this work with those reported in recent literature. (e) The digital photos of the Zn electrodes mentioned in ((b) and (c)), scale bars = 0.4 cm. ((f) and (g)) SEM images of the Zn electrodes after 100 cycles in Zn||Zn cells with (f) the Zn-$Mg(BBI)_2$ and (g) Zn-$Zn(BBI)_2$ electrolytes.

related peaks is suppressed in the patterns from the Zn-$MgSO_4$ and Zn-$Zn(BBI)_2$ electrolytes, which can be ascribed to the electrostatic shielding effect of Mg^{2+} and the protective interfacial adsorption of BBI^-, respectively [17, 22–24]. However, extending the cycling from 25 to 100 cycles (Fig. 2(a)) reveals a critical divergence in texture stability. The $RTC_{(002)}$ for the Zn-$Zn(BBI)_2$ electrolyte decreased from 97.8% to 74.6% (Fig. S8 in the ESM). This degradation is likely initiated by the accumulation of impurity phases (e.g., ZSH) and non-(002) Zn grains, which act as heterogeneous nucleation sites and ultimately lead to the growth of randomly oriented flakes, as morphologically observed in Fig. 1(g). In contrast, the Zn electrode cycled in the Zn-$Mg(BBI)_2$ electrolyte maintained a high $RTC_{(002)}$ of 97.3% after 100 cycles with no detectable impurity phases [25]. It reveals the dual functionality of Mg^{2+} in concurrently mitigating side reactions and stabilizing the preferred crystallographic texture over extended cycling.

The corrosion behavior of Zn electrodes in the different electrolytes was evaluated using Tafel polarization measurements (Fig. 2(b)). The two BBI-containing electrolytes significantly suppressed the corrosion current density (i_{corr}) and shifted the corrosion potential (E_{corr}) to a more positive value compared to the values tested in the $ZnSO_4$ electrolyte (Figs. S9 and S10 in the ESM), demonstrating a marked improvement in both the kinetic and thermodynamic resistance to corrosion [26, 27]. To elucidate the underlying mechanisms, we characterized the bulk properties of the electrolytes. The ^1H nuclear magnetic resonance (^1H NMR) spectrum of the $ZnSO_4$ electrolyte showed a downfield chemical shift of water protons (δ = 5.11 ppm) relative to pure water (δ = 4.80 ppm), indicating the solvation of Zn^{2+} [28, 29]. This shift was unaffected by the addition of $MgSO_4$ but was further enhanced in the Zn-$Zn(BBI)_2$ (5.17 ppm) and Zn-$Mg(BBI)_2$ (5.16 ppm) electrolytes (Fig. 2(c)), which suggests that BBI^- induces a reorganization of the H-bond networks, which can be attributed to the formation of new H-bonds between water molecules and the

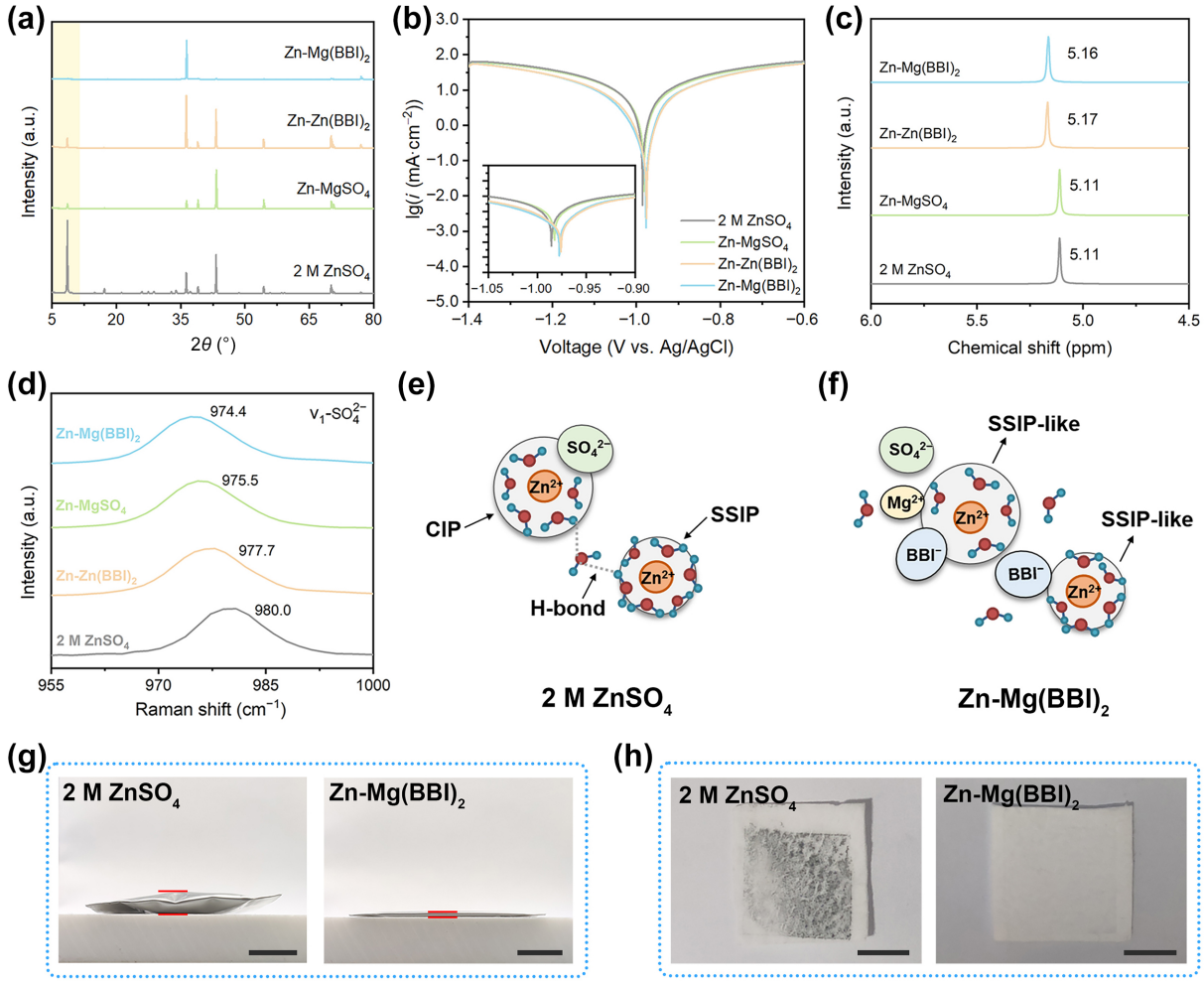

Figure 2 Suppression of corrosion and side reactions in the Zn-Mg(BBI)$_2$ electrolyte. (a) XRD patterns of Zn electrodes after 100 cycles in Zn||Zn symmetric cells (5 mA·cm^{-2} and 5 mAh·cm^{-2}) with the four different electrolytes. ((b)–(d)) Electrochemical and spectroscopic characterizations of the electrolytes: (b) Tafel polarization curves, (c) ^{1}H NMR spectra, and (d) Raman spectra focusing on the ν_1-SO_4^{2-} band. ((e) and (f)) Schematic illustrations proposing the dominant solvation structures in (e) the $ZnSO_4$ and (f) Zn-Mg(BBI)$_2$ electrolytes. ((g) and (h)) Digital photos of (g) pouch-type Zn||Zn cells and (h) their corresponding separators after 50 cycles in the $ZnSO_4$ and Zn-Mg(BBI)$_2$ electrolytes under the same cycling conditions. Scale bars = 1 cm.

polar functional groups of the anion. Complementing these findings, diffusion-ordered spectroscopy (DOSY) revealed that the addition of Mg(BBI)$_2$ led to a slight decrease in the diffusion coefficient of water (6.93×10^{-10} m^2·s^{-1}) compared to the values in the $ZnSO_4$ and Zn-$MgSO_4$ electrolytes (both 6.96×10^{-10} m^2·s^{-1}). This more restricted water mobility in the Mg(BBI)$_2$-containing electrolyte contributes to the suppression of water-induced side reactions at the Zn interface.

Based on the Eigen–Tamm mechanism, $ZnSO_4$ solvation in aqueous electrolytes primarily involves two distinct models: the solvent-separated ion pair (SSIP), typified by the well-dissociated structure $[Zn^{2+}(H_2O)_6]SO_4^{2-}$, and the contact ion pair (CIP), represented by the partly dissociated $Zn^{2+}(H_2O)_5OSO_3^{2-}$ [30]. Raman spectroscopy focusing on the ν_1-SO_4^{2-} band was used to probe these ion associations (Fig. 2(d)). Compared to the $ZnSO_4$ electrolyte, the ν_1-SO_4^{2-} bands in the Zn-$MgSO_4$, Zn-Zn(BBI)$_2$, and Zn-Mg(BBI)$_2$ electrolytes all shift to lower wavenumbers. This consistent red shift indicates a weakened association between Zn^{2+} and SO_4^{2-}, favoring a solvation structure closer to the SSIP model [31]. Notably, the Zn-Mg(BBI)$_2$ electrolyte exhibits the band located at the lowest wavenumber (974.4 cm^{-1}), illustrating the most effective disruption of the CIP structure, thereby minimizing the direct participation of SO_4^{2-} in interfacial side reactions with the Zn electrode. Integrating these findings with the prior NMR and DOSY results, schematic models of the solution structures in the $ZnSO_4$ and Zn-Mg(BBI)$_2$ electrolytes are proposed in Figs. 2(e) and 2(f), respectively. Mg^{2+} in the Zn-Mg(BBI)$_2$ electrolyte could continuously suppress parasitic reactions by weakening Zn^{2+}-SO_4^{2-}/H_2O interactions, thereby avoiding the formation of non-(002) heterogeneous nucleation sites to sustain the well-defined (002)-textured structure over extended cycling. The practical consequence of this stabilized interface is visually confirmed by digital photos of the pouch-type Zn||Zn cells using Mg(BBI)$_2$ and their separators after 50 cycles (5 mA·cm^{-2} and 5 mAh·cm^{-2}). As shown in Figs. 2(g) and 2(h), the cell using the Zn-Mg(BBI)$_2$ electrolyte shows a clear suppression of gas generation and the formation of "dead Zn" compared to the cell using the $ZnSO_4$ electrolyte. This improvement arises from two synergistic factors: (i) The SSIP-like solvation suppresses side reactions, ensuring a cleaner interface for more complete Zn stripping; and (ii) the sustained (002)-textured deposition promotes a smooth and compact morphology with uniform current distribution. These effects minimize the formation of electronically disconnected Zn debris on the separator.

2.3 Long-term plating/stripping reversibility

The electrochemical cycling stability of Zn electrodes was first evaluated in coin-type Zn||Zn symmetric cells. As shown in Fig. 3(a), the cell using the Zn-Mg(BBI)$_2$ electrolyte achieved an exceptional cycle life of more than 4000 h at 1 mA·cm^{-2} and 1 mA·cm^{-2} (2.1% ZUR) without failure. Under identical conditions, Zn||Zn cells using bare $ZnSO_4$, Zn-$MgSO_4$, and Zn-Zn(BBI)$_2$ electrolytes experienced short circuits after ~ 228, ~ 217, and ~ 2488 h, respectively (Fig. 3(a) and Fig. S11 in the ESM). At 5 mA·cm^{-2} and 5 mAh·cm^{-2} (10.4% ZUR), the Zn||Zn cell using the Zn-Mg(BBI)$_2$ electrolyte again delivered a significantly extended cycling lifespan of over 1400 h, which is far longer than those of the cells using $ZnSO_4$ (~ 108 h), Zn-$MgSO_4$ (~ 125 h), and Zn-Zn(BBI)$_2$ (~ 545 h) electrolytes (Fig. 3(b) and Fig. S12 in the ESM). To further assess the stability under harsh conditions, Zn||Zn cells assembled with ultrathin Zn electrodes (10 μm in thickness) were tested at 1 mA·cm^{-2} and 5 mAh·cm^{-2}, corresponding to a high ZUR of 85.4% (Fig. S13 in the ESM). The Zn||Zn cell using Mg(BBI)$_2$ additive sustained stable operation for > 300 h, which stands in stark contrast to the rapid failure (~ 20 h) observed with bare $ZnSO_4$ electrolyte. The capability of this hybrid additive in promoting long-term stability is clearly demonstrated when benchmarked against recent literature, as summarized in Table S2 in the ESM. Complementing the galvanostatic cycling tests, the Zn plating process was visually monitored in real-time, accomplished using a transparent Zn||Zn cell subjected to a one-hour plating step at a high current density of 20 mA·cm^{-2}. The *in-situ* optical microscopy images reveal a remarkably smooth and uniform Zn surface in the Zn-Mg(BBI)$_2$ electrolyte (Fig. 3(c)). However, rough and irregular deposits formed in bare $ZnSO_4$, Zn-$MgSO_4$, and Zn-Zn(BBI)$_2$ electrolytes (Fig. 3(d) and Fig. S14 in the ESM), providing evidence that the Mg(BBI)$_2$ additive more effectively suppresses dendritic growth.

The cycling reversibility of Zn electrodes was further evaluated by testing the Coulombic efficiency (CE) in Zn||Cu cells (Fig. 3(e)). At 4 mA·cm^{-2} and 4 mAh·cm^{-2} (with a cut-off charge voltage of 0.7 V), the Zn||Cu cell using bare $ZnSO_4$ electrolyte maintained stable operation for only ~ 100 cycles before rapid failure. Although the introduction of Zn(BBI)$_2$ extended the cycle life to ~ 300 cycles, it failed to ensure long-term reversibility, as indicated by significant fluctuations in the CE values. Fortunately, the cell using the Zn-Mg(BBI)$_2$ electrolyte exhibited highly reversible Zn plating/stripping for over 600 cycles, achieving a high average CE of 99.8%. According to the initial charge/discharge profiles (Figs. S15–S17 in the ESM), the Zn||Cu cell using the Zn-Mg(BBI)$_2$ electrolyte could exhibit the highest CE of 98.99%, outperforming those of the cells using bare $ZnSO_4$ (96.87%) and Zn-Zn(BBI)$_2$ (96.48%) electrolytes. Furthermore, the Zn-Mg(BBI)$_2$ electrolyte benefited from the lowest nucleation overpotential (0.069 V, Fig. 3(f)), which facilitates a reduced energy barrier for Zn grain growth. Additionally, the optimized concentration of the bulky BBI^- anion in the Zn-Mg(BBI)$_2$ electrolyte (0.04 M) is substantially lower than that in our previous report, weakly solvating 1 M Zn(BBI)$_2$ electrolyte (2 M

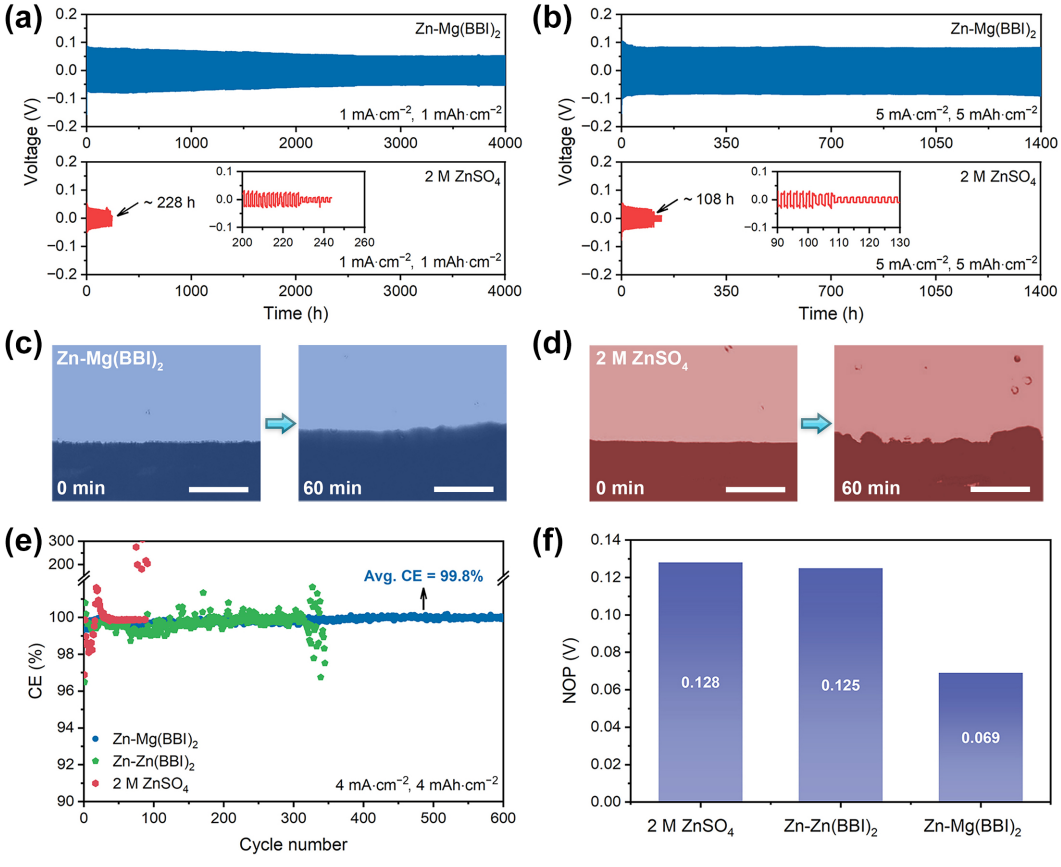

Figure 3 Electrochemical performance of Zn electrodes in symmetric and asymmetric cells using the Zn-Mg(BBI)$_2$ electrolyte. ((a) and (b)) Galvanostatic cycling profiles of Zn||Zn symmetric cells using bare $ZnSO_4$ and Zn-Mg(BBI)$_2$ electrolytes at (a) 1 and (b) 5 mA·cm^{-2}. ((c) and (d)) *In-situ* optical microscopy images captured in transparent Zn||Zn cells after 1-h plating at 20 mA·cm^{-2} in (c) Zn-Mg(BBI)$_2$ and (d) bare $ZnSO_4$ electrolytes (scale bars: 80 μm). (e) CEs of Zn||Cu asymmetric cells using bare $ZnSO_4$, Zn-Zn(BBI)$_2$, and Zn-Mg(BBI)$_2$ electrolytes at 4 mA·cm^{-2} and 4 mAh·cm^{-2}. (f) Initial nucleation overpotential of the Zn||Cu cells.

BBI^- anion) [19]. As summarized in Table S3 in the ESM, this lower dosage effectively reduces the polarization in Zn||Zn cells and ensures excellent orientation selectivity for the electrodeposited Zn, as corroborated by the data in Fig. S18 in the ESM.

2.4 Working mechanism of bifunctional $Mg(BBI)_2$

The interfacial characteristics at the Zn electrode in different electrolytes were firstly investigated through contact angle measurements and electric double-layer capacitance (EDLC), with the key results summarized in Fig. 4(a). As shown in Fig. S19 in the ESM, the contact angles for the $ZnSO_4$|Zn and Zn-$MgSO_4$|Zn interfaces were nearly identical, measuring at 88.0° and 87.5°, respectively. In contrast, the interface with the Zn-$Mg(BBI)_2$ electrolyte displayed a significantly reduced contact angle of 56.0°. This enhanced wettability is attributed to the adsorption of the amphiphilic BBI^- anion, which features both hydrophobic benzene rings (–Ph) and hydrophilic sulfonimide groups (–SO_2–N–SO_2–). EDLC analysis (Fig. S20 in the ESM) further revealed interfacial differences, illustrating a value of 36.6 μF·cm^{-2} for the Zn-$Mg(BBI)_2$ electrolyte, which is larger than those for the $ZnSO_4$ (23.6 μF·cm^{-2}) and Zn-$MgSO_4$ (26.8 μF·cm^{-2}) electrolytes. The increased capacitance indicates that the synergistic interaction between BBI^- anions and Mg^{2+} cations effectively restructures the structure of the electric double layer [32]. As a result, the highly active sites on the Zn surface could be sheltered by BBI^-, enforcing Zn^{2+} adsorption onto sites with weaker thermodynamic activity, such as the Zn(002) plane, thereby promoting a more uniform deposition morphology [33].

The spatial distribution of BBI^- on the Zn electrode was precisely mapped using nano-infrared (nano-IR) spectroscopy, a high-resolution infrared imaging technique based on atomic force microscopy (AFM). Figure 4(b) shows the AFM image of a Zn electrode cycled in the Zn-$Mg(BBI)_2$ electrolyte, revealing a grain composed of multilayer (002)-oriented Zn nanosheets. Figure 4(c) is the nano-IR overlap of the selected region at ~ 1450 cm^{-1}, which corresponds to the C=C stretching vibration of the aromatic ring [34, 35]. The intensity of the C=C signal was unevenly distributed, with stronger signals (warm-toned regions) localized at the edges of

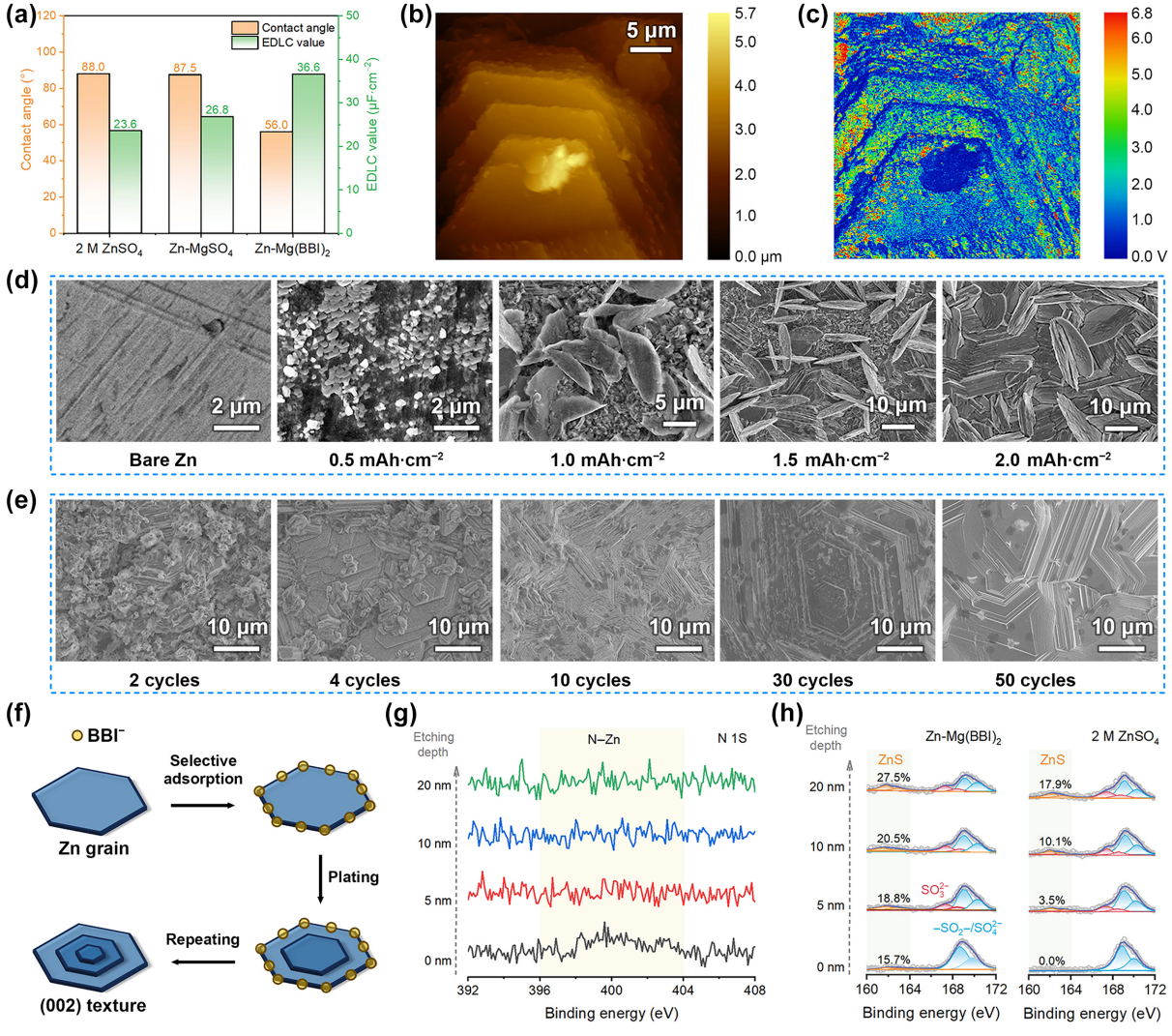

Figure 4 Mechanism of region-selective Zn electrodeposition regulated by $Mg(BBI)_2$. (a) Interfacial properties (contact angles and EDLC values) measured in different electrolytes. ((b) and (c)) Nano-IR characterization of the Zn electrode after 50 cycles (5 mA·cm^{-2} and 5 mAh·cm^{-2}): (b) AFM image of Zn flakes and (c) corresponding C=C signal distribution. (d) *Ex-situ* SEM images of the cycled Zn electrodes with a total plating areal capacity of 2 mAh·cm^{-2}. (e) SEM images of Zn electrodes after 2, 4, 10, 30, and 50 cycles in Zn-$Mg(BBI)_2$ electrolyte. (f) Schematic model of region-selective deposition. ((g) and (h)) XPS depth profiles after 50 cycles (5 mA·cm^{-2} and 5 mAh·cm^{-2}): (g) N 1s profiles of the electrode cycled in Zn-$Mg(BBI)_2$ electrolyte and (h) S 2p profiles of the electrode cycled in bare $ZnSO_4$ and Zn-$Mg(BBI)_2$.

the hexagonal nanosheets, in contrast to the weaker signals (cool-toned regions) at their centers. This spatial contrast indicated the preferential adsorption of BBI^- on non-(002) facets, suggesting the role as a site-blocking agent that promotes (002)-dominated Zn deposition. To further elucidate the crystallographic dependence of electrochemical activity, we performed another spatially resolved characterization using *in-situ* scanning electrochemical cell microscopy (SECCM), which enables real-time visualization of localized electrodeposition behavior. The SECCM system consisted of a Zn electrode after 50 cycles in the Zn-$Mg(BBI)_2$ electrolyte (5 $mA{\cdot}cm^{-2}$ and 5 $mAh{\cdot}cm^{-2}$) and a position-controlled probe filled with the same electrolyte, forming a submicron-sized droplet at its tip for localized electrochemical mapping. As shown in Figs. S21(a) and S21(b) in the ESM, the SECCM images of a representative structural unit, composed of stacked (002)-oriented Zn hexagons, revealed significantly lower current at the edges of the nanosheets compared to their central regions. This result demonstrated markedly suppressed Zn deposition kinetics at the edges, consistent with the preferential adsorption of BBI^- identified by nano-IR. Furthermore, the Zn electrode exhibited negligible electrodeposition activity in regions not exposed in the (002) orientation (Figs. S21(c) and S21(d) in the ESM), proving the kinetic heterogeneity of the Zn deposition process.

Ex-situ morphological characterization was performed to trace the structural evolution of Zn electrodeposits in the Zn-$Mg(BBI)_2$ electrolyte. As illustrated in Fig. 4(d), Zn electrodes were collected from Zn||Zn cells subjected to galvanostatic plating (1 $mA{\cdot}cm^{-2}$) with a capacity interval of 0.5 $mAh{\cdot}cm^{-2}$. In the early stages of deposition, numerous flake-like Zn grains were formed and preferentially distributed across the electrode surface. As deposition proceeded, these grains gradually evolved into horizontally oriented and partially transformed into an incomplete hexagonal structure. The enrichment of BBI^- at the edges of these flakes promoted Zn^{2+} deposition in the center regions. The further growth and stacking ultimately led to the formation of a highly (002)-textured Zn plating. Moreover, this oriented electrodeposition also induced a gradual reconstruction of the Zn electrode surface. Figure 4(e) exhibits the SEM images of the Zn electrodes after complete 2, 4, 10, 30, and 50 plating/stripping cycles in the Zn-$Mg(BBI)_2$ electrolyte. The surface morphology progressively became smoother with increasing cycle number, clearly revealing the horizontal hexagonal feature of the (002) plane. After only 10 cycles, the surface was reconstructed with a dominant (002) texture, which subsequently facilitated epitaxial Zn deposition. Based on these results, a schematic model was constructed to summarize the region-selective electrodeposition process driven by BBI^- adsorption, as depicted in Fig. 4(f).

Depth-profiling X-ray photoelectron spectroscopy (XPS) was employed to analyze the surface composition of Zn electrodes after cycling in the $ZnSO_4$ and the Zn-$Mg(BBI)_2$ electrolyte. The Mg 1s depth profile for the electrode cycled in the Zn-$Mg(BBI)_2$ electrolyte (Fig. S22 in the ESM) showed no detectable Mg signal in the top 20 nm surface region, indicating that Mg^{2+} participates primarily in the solvation structure of Zn^{2+} without forming any Mg-containing compounds on the electrode surface. Furthermore, the N 1s spectra (Fig. 4(g)) displayed a characteristic N–Zn peak at ~ 399.5 eV, which diminished rapidly with increasing Ar^+ sputtering depth. This trend confirms the adsorption of BBI^- primarily within the near-surface Zn layer. The S 2p depth profiles (Fig. 4(h)) revealed a notably higher content of ZnS (~ 161.5 eV) on the electrode cycled in the Zn-$Mg(BBI)_2$ electrolyte compared to that in the $ZnSO_4$ electrolyte. This result indicates that BBI^- promotes the formation of ZnS species, which are known to function as a protective inorganic layer for Zn electrodes [32].

Density functional theory (DFT) calculations and molecular dynamics (MD) simulations were conducted to further investigate the working mechanism of the $Mg(BBI)_2$ additive. DFT results (Fig. 5(a) and Fig. S23 in the ESM) reveal that BBI^- exhibits the highest adsorption energy (E_{ads}) of −1.292 eV on the (002) Zn plane, which is higher than that on the (100) (−4.798 eV) and (101) (−3.529 eV) planes. This indicates the stronger adsorption of BBI^- on the (100) and (101) planes. The unique selective adsorption blocks active sites on the non-(002) planes, thereby inhibiting Zn^{2+} deposition on these planes and indirectly guiding preferential growth along the (002) orientation. MD simulations provide further insight into the solvation structure. A snapshot of the equilibrated Zn-$Mg(BBI)_2$ electrolyte (Fig. S24 in the ESM) and the corresponding radial distribution functions (RDFs, Fig. 5(b)) confirm the participation of both Mg^{2+} and BBI^- in the Zn^{2+} solvation sheath. Specifically, Zn^{2+} coordinates closely with H_2O and BBI^-, as evidenced by the two distinct peaks for Zn–O (H_2O) and Zn–O (BBI^-) at 2.15 Å. More importantly, the distance between Zn^{2+} and O (SO_4^{2-}) in Zn-$Mg(BBI)_2$ electrolyte is 2.85 Å, which is notably larger than 2.42 Å observed in the $ZnSO_4$ electrolyte (from our previous work) [36]. This result matches well with the red shift of the ν_1-SO_4^{2-} band in the Raman spectra (Fig. 2(d)), collectively proving that the $Mg(BBI)_2$ additive facilitates the transition of the solvation structure from CIP to SSIP. Coordination number analysis (Fig. 5(c)) further reveals that the inner solvation shell of Zn^{2+} in the Zn-$Mg(BBI)_2$ electrolyte contains only three water molecules, fewer than the typical six in the $ZnSO_4$ electrolyte. This SSIP-type solvation structure, characterized by a weakened Zn^{2+}-SO_4^{2-} interaction and a reduced number of water molecules, effectively suppresses side reactions. Based on these findings, the working mechanism of the hybrid $Mg(BBI)_2$ additive can be summarized as follows (illustrated as Figs. 5(d) and 5(e)):

(1) BBI^- acts as a masking molecule, preferentially adsorbing on Zn(100) and Zn(101) and blocking nucleation sites on the two planes, kinetically promoting Zn deposition toward (002)-oriented growth;

(2) Mg^{2+} restructures the Zn^{2+} solvation from CIP to SSIP, mitigating the corrosivity of H_2O and SO_4^{2-} toward Zn electrodes and thereby preventing corrosion-induced texture degradation.

2.5 Practicality evaluation in AZMBs

To evaluate the practical applicability of the Zn-$Mg(BBI)_2$ electrolyte, Zn||VS_2 full cells were first assembled and tested. The VS_2 cathode material was synthesized via a hydrothermal method according to a previous report [37], confirmed by XRD (PDF #89-1640, Fig. S25 in the ESM). As shown in Fig. S26 in the ESM, the cyclic voltammetry (CV) curves of the cell, measured at 0.1 $mV{\cdot}s^{-1}$, displayed the characteristic redox behaviors of VS_2 cathodes [36, 37]. The rate performance of the Zn||VS_2 full cells using the Zn-$Mg(BBI)_2$ and $ZnSO_4$ electrolytes is compared in Fig. 6(a) (with corresponding charge/discharge curves shown in Figs. S27 and S28 in the ESM), indicating that the addition of 0.02 M $Mg(BBI)_2$ has a negligible impact on the specific capacity. More importantly, the long-term cycling tests (Fig. 6(b), and Figs. S29 and S30 in the ESM) clearly demonstrated the beneficial effect of the $Mg(BBI)_2$ additive. The cell cycled in the $ZnSO_4$ electrolyte quickly failed after

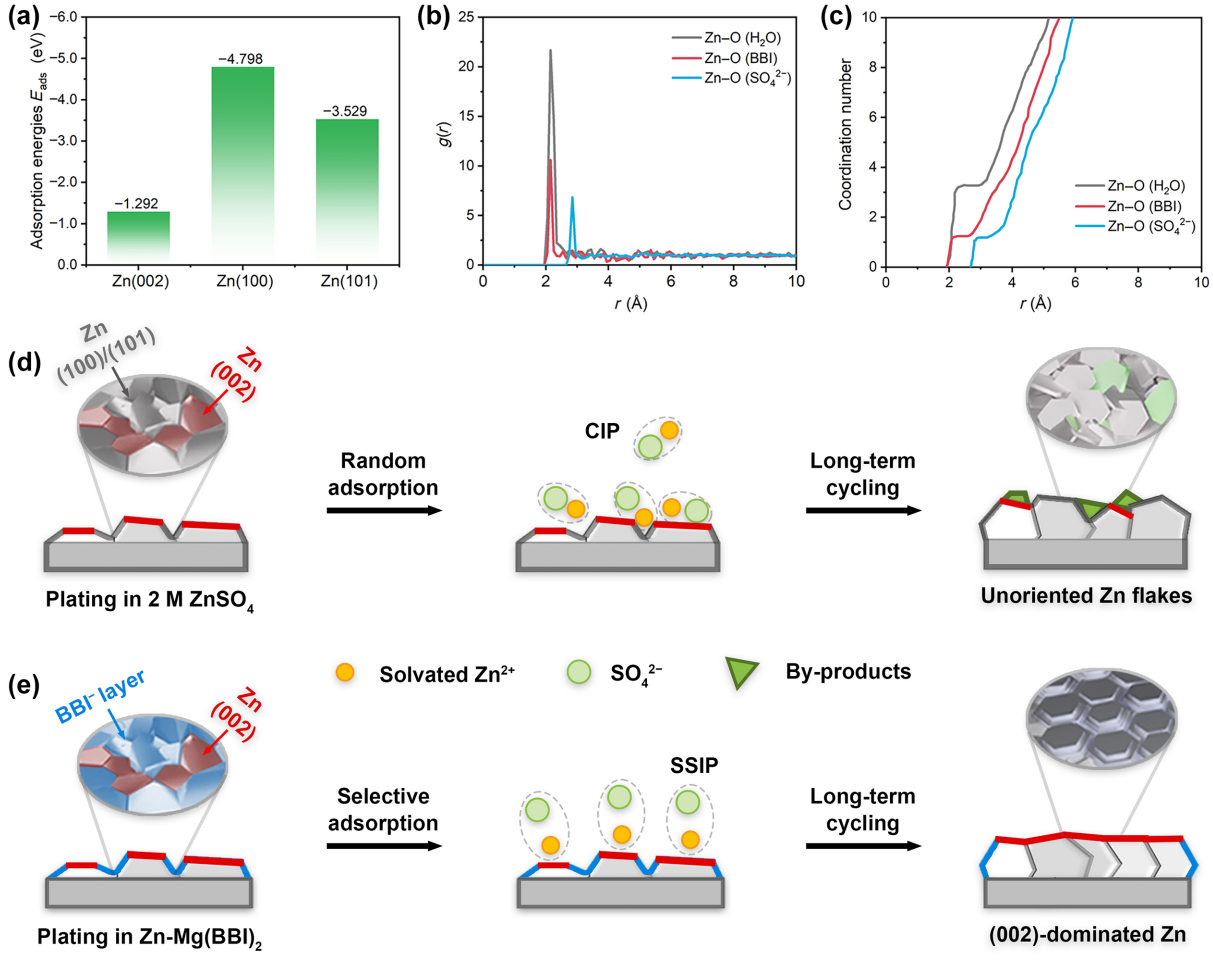

Figure 5 Theoretical insights into the Zn-Mg$(BBI)_2$ electrolyte. (a) Calculated adsorption energies of BBI^- on (002)-, (100)-, and (101)-exposed Zn facets. (b) Radial distribution functions for Zn–O pairs from H_2O, BBI^-, and SO_4^{2-} in the Zn-Mg$(BBI)_2$ electrolyte. (c) Coordination numbers of Zn^{2+} with O from H_2O, BBI^-, and SO_4^{2-}. ((d) and (e)) Schematic diagrams illustrating the Zn plating process in (d) the $ZnSO_4$ and (e) Zn-Mg$(BBI)_2$ electrolytes.

only ~ 320 cycles, whereas the cell cycled in the Zn-Mg$(BBI)_2$ electrolyte maintained stable operation for 1000 cycles at 1 A·g^{-1}, with a capacity retention of 72.8% and a high average CE of 99.9% (Fig. S31 in the ESM). Figure 6(c) shows the digital photos of the cycled Zn anodes disassembled from the Zn||VS_2 full cells after 1000 cycles. The Zn surface from the $ZnSO_4$ electrolyte is rough and fully covered by by-products. Fortunately, the Zn anode from the Zn-Mg$(BBI)_2$ electrolyte remained structurally intact with a smooth surface. Furthermore, XRD and SEM characterizations (Figs. S32–S34 in the ESM) confirmed that the hybrid additive could ensure a sustained (002)-dominated texture ($RTC_{(002)}$ = 95.7%) over 1000 cycles without severe corrosion.

The enhanced cycling stability enabled by the Zn-Mg$(BBI)_2$ electrolyte was further verified in full cells assembled with CVO cathodes. The CVO active material was synthesized using a modified oil-bath method [38], and its phase purity and morphology were confirmed by XRD and SEM analysis (Figs. S35 and S36 in the ESM, respectively). Figure 6(d) presents the long-term cycling performance of the Zn||CVO cells with a low cathode loading of ~ 0.9 mg·cm^{-2} at 1 A·g^{-1}. The cell using the Zn-Mg$(BBI)_2$ electrolyte achieved a superior capacity retention of 84.6% after 1000 cycles, significantly outperforming the 67.2% retention of the cell cycled in bare $ZnSO_4$ electrolyte. The corresponding 1000th-cycle charge/discharge profiles are compared in Fig. 6(e). This performance advantage in the Zn-Mg$(BBI)_2$ electrolyte was maintained under more practical testing conditions. Using a high-loading CVO cathode (~ 16 mg·cm^{-2}), the Zn||CVO full cell cycled in the Zn-Mg$(BBI)_2$ electrolyte delivered stable cycling over 800 cycles at 0.5 A·g^{-1} with a capacity retention of 76.9% (Fig. 6(f)). Notably, it exhibited negligible capacity decay over the last 600 cycles. In sharp contrast, the cell cycled in the $ZnSO_4$ electrolyte suffered a rapid capacity plummet after ~ 300 cycles. Even when the CVO loading was further increased to ~ 22.6 mg·cm^{-2}, the cell with the modified electrolyte still exhibited a specific discharge capacity of 89.0 mAh·g^{-1} after 100 cycles, corresponding to a high capacity retention of 81.0% (Fig. 6(g)). To demonstrate the practical viability of the hybrid additive beyond coin-type cells, pouch Zn||CVO cells with an active area of 3 cm × 3 cm and a cathode loading of ~ 12 mg·cm^{-2} were assembled and tested at 0.4 A·g^{-1} (Fig. 6(h)). A light board could be powered by the three series-connected Zn||CVO pouch cells, as shown in Fig. 6(i). Furthermore, the universality of the additive was confirmed in Zn||PANI full cells, which also showed enhanced electrochemical performance (Figs. S37 and S38 in the ESM).

3 Conclusions

In summary, this work presents a rationally designed organic-

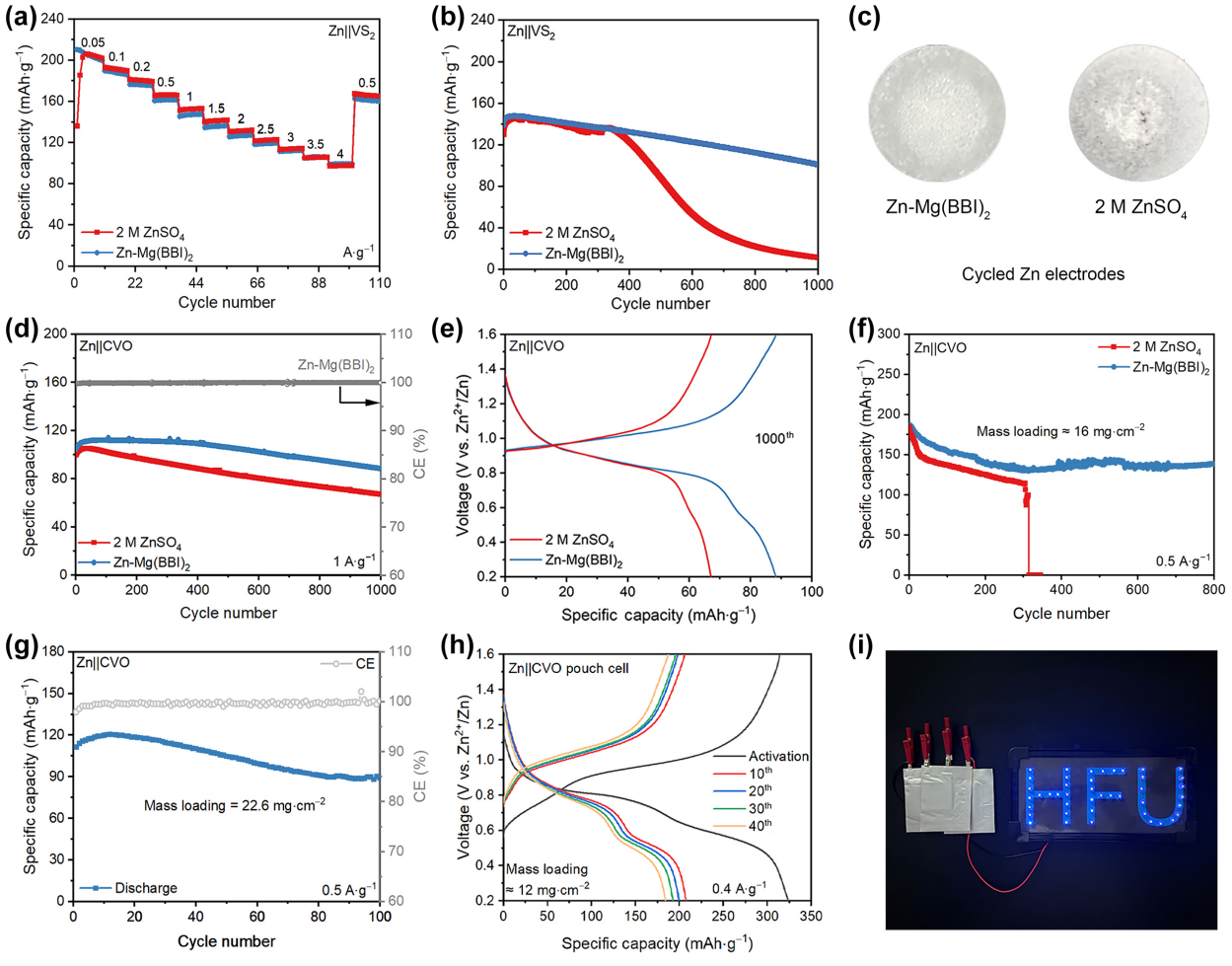

Figure 6 Full-cell electrochemical performance using the Zn-Mg(BBI)$_2$ electrolyte. (a) Rate performance and (b) cycling stability of Zn||VS$_2$ cells with low-mass-loading cathodes (~ 2 mg·cm^{-2}). (c) Photographs of the Zn anodes disassembled from Zn||VS$_2$ cells after 1000 cycles at 1 A·g^{-1}. (d) Long-term cycling performance and (e) the 1000th charge/discharge curves of Zn||CVO cells with low-loading cathodes (~ 0.9 mg·cm^{-2}). ((f) and (g)) Cycling performance of Zn||CVO cells with high-mass-loading cathodes at 0.5 A·g^{-1}: (f) ~ 16 and (g) ~ 22.6 mg·cm^{-2}. (h) Charge/discharge curves of a Zn||CVO pouch cell (CVO loading: ~ 12 mg·cm^{-2}) using the Zn-Mg(BBI)$_2$ electrolyte at 0.4 A·g^{-1}. (i) A light board powered by three series-connected Zn||CVO pouch cells.

inorganic hybrid molecule, Mg(BBI)$_2$, as a bifunctional electrolyte additive that simultaneously achieves long-acting and single-textured Zn electrodeposition. The BBI$^-$ anions serve as a texture-regulating agent to block the nucleation sites on (101) and (100) planes, thereby kinetically suppressing the electrodeposition process toward non-(002)-oriented growth. Concurrently, Mg^{2+} cations and BBI$^-$ anions cooperatively reconfigure the primary solvation shell of Zn^{2+}, transforming the coordination structure from CIP to SSIP, which effectively mitigates the corrosive activity of the electrolyte. This dual-regulation mechanism enables the formation of Zn deposits featuring an ultrahigh RTC$_{(002)}$ of 97.9% and suppresses the parasitic reactions, which endows exceptional electrochemical durability of high-capacity AZMBs. This molecular-level design paradigm provides a promising research direction for electrolyte engineering, promoting the development of durable AZMBs for next-generation energy storage devices.

Electronic Supplementary Material: Supplementary material (experimental section, additional figures, and additional tables) is available in the online version of this article at https://doi.org/10.26599/NR.2026.94908661.

Data availability

All data needed to support the conclusions in the paper are presented in the manuscript and the Electronic Supplementary Material. Additional data related to this paper may be requested from the corresponding author upon request.

Acknowledgements

This work was supported by the National Natural Science Foundation of China (No. 22409049), the Fundamental Research Funds for the Central Universities (No. 2021GCRC001), the Natural Science Research Project for Anhui Provincial Universities (Nos. 2024AH051520, 2022AH010096, 2024AH051531, and 2024AH051529), the Talent Scientific Research Foundation of Hefei University (No. 24RC37), the University Synergy Innovation Program of Anhui Province (No. GXXT-2023-024), the Project for Cultivating Academic (or Disciplinary) Leaders (No. DTR2023043), the Anhui Provincial Science and Technology Innovation Key Project Plan (No. 202423h08050005), and the Natural Science Foundation of Anhui Province (No. 2208085ME108). We also thank the Ceshigo Research Service Agency for the technical

support of theoretical calculations, and Eaglenos Sciences, Inc., for the technical support of SECCM.

Declaration of competing interest

All the contributing authors report no conflicts of interest in this work.

Author contribution statement

H. R. D.: Conceptualization, data curation, methodology, formal analysis, writing – original draft, writing – review & editing, funding acquisition, supervision. S. J. Z.: Investigation, data curation, formal analysis, methodology, writing – original draft. W. J. Y.: Data curation, funding acquisition. K. H. H.: Funding acquisition, resources. L. H.: Resources. X. F. Z.: Data curation. Y. Z.: Formal analysis. W. Y.: Resources. X. L.: Funding acquisition, data curation, supervision. L. Q.: Conceptualization, formal analysis, funding acquisition, writing – review & editing, supervision. All the authors have approved the final manuscript.

Use of AI statement

None.

References

[1] Zhao, Y. J.; Wang, Y. Y.; Li, J. Z.; Xiong, J. W.; Li, Q.; Abdalla, K. K.; Zhao, Y.; Cai, Z.; Sun, X. M. Thermodynamic and kinetic insights for manipulating aqueous Zn battery chemistry: Towards future grid-scale renewable energy storage systems. *eScience* **2025**, *5*, 100331.

[2] Wang, T.; Tang, S. C.; Xiao, Y.; Xiang, W. W.; Yu, J. S. Strategies of interfacial chemistry manipulated zinc deposition towards high-energy and long-cycle-life aqueous anode-free zinc metal batteries. *Energy Environ. Sci.* **2025**, *18*, 545–578.

[3] Wang, T. R.; Chen, B.; Liu, Y. J.; Song, Z. Y.; Wang, Z. Q.; Chen, Y. W.; Yu, Q.; Wen, J. Y.; Dai, Y. M.; Kang, Q. et al. Fatigue of Li metal anode in solid-state batteries. *Science* **2025**, *388*, 311–316.

[4] Song, T. B.; Ma, Q. L.; Wang, B. J.; Zhang, X. R.; Wang, Y. G.; Xiong, H. M. High-capacity and long-life cathode constructed solely by carbon dots for aqueous zinc-ion batteries. *Angew. Chem., Int. Ed.* **2025**, *64*, e202503655.

[5] Ma, Q. L.; Zhang, X. R.; Wang, B. J.; Sun, H. W.; Xiong, H. M. Anode interface layers constructed *in situ* by multifunctional carbon dots for ultra-stable aqueous zinc-ion batteries. *Chem. Eng. J.* **2026**, *529*, 172570.

[6] Li, Y. H.; Ren, X. Y.; Zhang, D. W.; Ju, S. H.; Hu, W.; Hang, T.; Li, M.; Wu, Y. W. Dendrites-free Zn anode enabled by dense Zn deposition and spontaneous texture reconstruction on (110)-oriented nanotwinned Cu. *Adv. Funct. Mater.* **2026**, *36*, e14665.

[7] Zheng, J. X.; Zhao, Q.; Tang, T.; Yin, J. F.; Quilty, C. D.; Renderos, G. D.; Liu, X. T.; Deng, Y.; Wang, L.; Bock, D. C. et al. Reversible epitaxial electrodeposition of metals in battery anodes. *Science* **2019**, *366*, 645–648.

[8] Ma, Y. F.; Pepas, J.; Zhang, G. X.; Liu, Z. N.; Su, Y.; Bai, J. M.; Zhong, H.; Li, T. Y.; Xu, W. Q.; Kang, M. J. et al. Understanding rate-dependent textured growth in zinc electrodeposition via high-throughput *in situ* x-ray diffraction. *Nat. Commun.* **2025**, *16*, 7448.

[9] Ji, J.; Zhu, Z. L.; Du, H. R.; Qi, X. Q.; Yao, J.; Wan, H. Z.; Wang, H.; Qie, L.; Huang, Y. H. Zinc-contained alloy as a robustly adhered interfacial lattice locking layer for planar and stable zinc electrodeposition. *Adv. Mater.* **2023**, *35*, 2211961.

[10] Tian, X. M.; Sun, Y.; Li, H.; Duan, X. G.; Zhao, Q.; Ma, T. Y. Crystallographic texturing of electrodeposits for sustainable Zn anodes. *Adv. Energy Mater.* **2025**, *15*, 2403995.

[11] Zhang, X. T.; Li, J. X.; Wang, T. Q.; Gong, Y. X.; Zhou, J. Uniaxially oriented zinc metal negative electrodes toward spontaneous dislocation-free homoepitaxy. *Nat. Commun.* **2025**, *16*, 5781.

[12] Liu, H. Y.; Sun, H. H.; Hua, W.; Liu, X. J.; Liu, W. B.; Wang, J. G. Roll-to-roll coating to processing large-area zinc anodes toward fast and dendrite-free deposition. *Adv. Funct. Mater.* **2025**, *35*, e09206.

[13] Zhao, Y. X.; Guo, S.; Chen, M. J.; Lu, B. G.; Zhang, X. T.; Liang, S. Q.; Zhou, J. Tailoring grain boundary stability of zinc-titanium alloy for long-lasting aqueous zinc batteries. *Nat. Commun.* **2023**, *14*, 7080.

[14] Chen, S.; Luo, Z.; Xia, Y. F.; Wu, X. X.; Wang, K. B.; Yan, M.; Pan, H. G.; Xu, B. B.; Jiang, Y. Z. Step-edge guided homoepitaxy enables highly reversible Zn plating/stripping. *Angew. Chem., Int. Ed.* **2025**, *64*, e202501176.

[15] Hu, Z. Q.; Zhang, F. L.; Zhao, Y.; Wang, H. R.; Huang, Y. X.; Wu, F.; Chen, R. J.; Li, L. A self-regulated electrostatic shielding layer toward dendrite-free Zn batteries. *Adv. Mater.* **2022**, *34*, 2203104.

[16] Ma, Q. L.; Song, T. B.; He, T. L.; Zhang, X. R.; Xiong, H. M. Sulfur-doped carbon dots: A novel bifunctional electrolyte additive for high-performance aqueous zinc-ion batteries. *Acta Phys. Chim. Sin.* **2025**, *41*, 100106.

[17] Xu, D. M.; Chen, B. Q.; Ren, X. T.; Han, C.; Chang, Z.; Pan, A. Q.; Zhou, H. S. Selectively etching-off the highly reactive (002) Zn facet enables highly efficient aqueous zinc-metal batteries. *Energy Environ. Sci.* **2024**, *17*, 642–654.

[18] Zhang, Z. C. Y.; Wang, P.; Wei, C. L.; Feng, J. K.; Xiong, S. L.; Xi, B. J. Synchronous regulation of D-band centers in Zn substrates and weakening Pauli repulsion of Zn ions using the ascorbic acid additive for reversible zinc anodes. *Angew. Chem., Int. Ed.* **2024**, *63*, e202402069.

[19] Du, H. R.; Dong, Y. H.; Li, Q. J.; Zhao, R. R.; Qi, X. Q.; Kan, W. H.; Suo, L. M.; Qie, L.; Li, J.; Huang, Y. H. A new zinc salt chemistry for aqueous zinc-metal batteries. *Adv. Mater.* **2023**, *35*, 2210055.

[20] Zhang, J. M.; Huang, W. W.; Li, L. W.; Chang, C. Y.; Yang, K.; Gao, L.; Pu, X. Nonepitaxial electrodeposition of (002)-textured Zn anode on textureless substrates for dendrite-free and hydrogen evolution-suppressed Zn batteries. *Adv. Mater.* **2023**, *35*, 2300073.

[21] Tian, C.; Wang, J. L.; Sun, R. X.; Ali, T.; Wang, H. F.; Xie, B. B.; Zhong, Y. J.; Hu, Y. Improved interfacial ion migration and deposition through the chain-liquid synergistic effect by a carboxylated hydrogel electrolyte for stable zinc metal anodes. *Angew. Chem., Int. Ed.* **2023**, *62*, e202310970.

[22] Wang, P. J.; Xie, X. S.; Xing, Z. Y.; Chen, X. H.; Fang, G. Z.; Lu, B. G.; Zhou, J.; Liang, S. Q.; Fan, H. J. Mechanistic insights of Mg^{2+}-electrolyte additive for high-energy and long-life zinc-ion hybrid capacitors. *Adv. Energy Mater.* **2021**, *11*, 2101158.

[23] Song, Y. X.; Wang, J.; Zhong, X. B.; Wang, K.; Zhang, Y. H.; Liu, H. T.; Zhang, L. X.; Liang, J. G.; Wen, R. Interfacial chemistry regulation via dibenzenesulfonamide-functionalized additives enables high-performance Zn metal anodes. *Energy Storage Mater.* **2023**, *58*, 85–93.

[24] Zhao, R. R.; Wang, H. F.; Du, H. R.; Yang, Y.; Gao, Z. H.; Qie, L.; Huang, Y. H. Lanthanum nitrate as aqueous electrolyte additive for favourable zinc metal electrodeposition. *Nat. Commun.* **2022**, *13*, 3252.

[25] He, X. F.; Cui, Y. L. S.; Qian, Y. C.; Wu, Y. D.; Ling, H. Y.; Zhang, H. R.; Kong, X. Y.; Zhao, Y.; Xue, M. Q.; Jiang, L. et al. Anion concentration gradient-assisted construction of a solid–electrolyte interphase for a stable zinc metal anode at high rates. *J. Am. Chem. Soc.* **2022**, *144*, 11168–11177.

[26] Song, T. B.; Huang, Z. H.; Zhang, X. R.; Ni, J. W.; Xiong, H. M. Nitrogen-doped and sulfonated carbon dots as a multifunctional additive to realize highly reversible aqueous zinc-ion batteries. *Small* **2023**, *19*, 2205558.

[27] Liu, J. B.; Gao, W. J.; Zhang, X. Y.; Li, J. H.; Li, Q.; Li, G. R.; Zhang,

Y. G.; Chen, Z. W. Rational construction of rich coordination-unsaturated Zr-BTB electrocatalyst towards advanced lithium-sulfur batteries. *Chem. Eng. J.* **2023**, *471*, 144238.

[28] Cao, L. S.; Li, D.; Hu, E. Y.; Xu, J. J.; Deng, T.; Ma, L.; Wang, Y.; Yang, X. Q.; Wang, C. S. Solvation structure design for aqueous Zn metal batteries. *J. Am. Chem. Soc.* **2020**, *142*, 21404–21409.

[29] Chang, N. N.; Li, T. Y.; Li, R.; Wang, S. N.; Yin, Y. B.; Zhang, H. M.; Li, X. F. An aqueous hybrid electrolyte for low-temperature zinc-based energy storage devices. *Energy Environ. Sci.* **2020**, *13*, 3527–3535.

[30] Yang, H. J.; Chang, Z.; Qiao, Y.; Deng, H.; Mu, X. W.; He, P.; Zhou, H. S. Constructing a super-saturated electrolyte front surface for stable rechargeable aqueous zinc batteries. *Angew. Chem., Int. Ed.* **2020**, *59*, 9377–9381.

[31] Rudolph, W. W.; Brooker, M. H.; Tremaine, P. R. Raman spectroscopy of aqueous $ZnSO_4$ solutions under hydrothermal conditions: Solubility, hydrolysis, and sulfate ion pairing. *J. Solution Chem.* **1999**, *28*, 621–630.

[32] Huang, C.; Zhu, D. J.; Zhao, X.; Hao, Y. S.; Yang, Y. J.; Qian, Y.; Chang, G.; Tang, Q. L.; Hu, A. P.; Chen, X. H. High-entropy-inspired multicomponent electrical double layer structure design for stable zinc metal anodes. *Angew. Chem., Int. Ed.* **2024**, *63*, e202411427.

[33] Lv, Y. Q.; Zhao, M.; Du, Y. D.; Kang, Y.; Xiao, Y.; Chen, S. M. Engineering a self-adaptive electric double layer on both electrodes for high-performance zinc metal batteries. *Energy Environ. Sci.* **2022**, *15*, 4748–4760.

[34] Abdul Qadir, M.; Ahmed, M.; Aslam, H.; Waseem, S.; Shafiq, M. I. Amidine sulfonamides and benzene sulfonamides: Synthesis and their biological evaluation. *J. Chem.* **2015**, *2015*, 524056.

[35] Tanaka, Y.; Tanaka, Y. Infrared spectra of bisarylsulfonimide derivatives. *Chem. Pharm. Bull.* **1974**, *22*, 2546–2551.

[36] Du, H. R.; Zhao, R. R.; Ji, J.; Qi, X. Q.; Wang, R.; Qie, L.; Huang, Y. H. Design of a permselective interface for highly stable Zn electrodeposition. *Energy Storage Mater.* **2023**, *54*, 461–468.

[37] Cui, Y. H.; Zhao, Q. H.; Wu, X. J.; Chen, X.; Yang, J. L.; Wang, Y. T.; Qin, R. Z.; Ding, S. X.; Song, Y. L.; Wu, J. W. et al. An interface-bridged organic–inorganic layer that suppresses dendrite formation and side reactions for ultra-long-life aqueous zinc metal anodes. *Angew. Chem., Int. Ed.* **2020**, *59*, 16594–16601.

[38] Li, M. Y.; Liu, X.; Wu, J.; Dong, X.; Wang, Y. D.; Passerini, S. Efficient and effective synthesis of $CaV_6O_{16}{\cdot}2.7H_2O$ as high-performance cathode material for aqueous zinc metal batteries. *Adv. Energy Mater.* **2025**, *15*, 2404037.